

ARTICLE OPEN



Intensification of heatwaves in China in recent decades: Roles of climate modes

Jia Wei^{1,2}, Weiqing Han³, Weiguang Wang^{1,2,4,5}✉, Lei Zhang^{6,7} and Balaji Rajagopalan⁸

Modes of climate variability can affect weather extremes, posing intractable challenges to our environment. However, to what extent climate modes can modulate heatwaves in China under a warming background remains poorly understood. Here, we examine the changes in heatwave intensity in seven distinct regions: three East, two middle, and two west regions over China and systematically explore the impacts of climate modes, by analyzing observations and performing model experiments using a Bayesian dynamic linear model and an atmospheric general circulation model (AGCM). Abrupt increases in heatwave intensity are detected across China during a transition period of 1993–2000, and the intensification remains robust in northern and western China after the warming trend being removed. The combined impacts of the El Niño–Southern Oscillation (ENSO), Atlantic Multidecadal Oscillation (AMO), and Indian Ocean Dipole (IOD) explain 62.35–70.01% of the observed heatwave intensification in East I, Middle I, West I, and West II regions. Decadal changes of atmospheric circulations associated with the negative phase transition of the Interdecadal Pacific Oscillation (IPO), which is highly correlated with the decadal variability of ENSO, combined with the positive phase transition of the AMO around the mid-1990s increase surface air temperature and enhance atmospheric internal variability and climate modes' impacts, resulting in the abrupt increase of heatwaves in the past two decades. These results highlight the importance of the concurrent phase transitions of decadal climate modes in regulating heatwaves.

npj Climate and Atmospheric Science (2023)6:98; <https://doi.org/10.1038/s41612-023-00428-w>

INTRODUCTION

Heatwaves have major impacts on ecosystems and human society¹. Historically, outbursts of heatwaves have been responsible for detrimental impacts on human health, crops, vegetation, air quality, and natural hazard^{2,3}. With the increase in global temperature due to climate change, heat extremes have occurred around the world and raised increasing public concerns in the past few decades^{4–10}. Overlying the warming trend, the dominant modes of climate variability—such as the El Niño and Southern Oscillation (ENSO), the Atlantic Multidecadal Oscillation (AMO), and the Indian Ocean Dipole (IOD)—have been shown to modulate global hydrometeorological regimes, intensify the duration and frequency of heatwaves, and induce natural disasters in various regions around the world^{11–16}. Despite a growing appreciation of the interplay between anthropogenic warming and internal climate modes, how strongly climate modes can modulate heatwaves in China is little known. In particular, our scientific understanding of the physical processes that lead to heatwave intensification is limited^{17,18}.

In the past century, China has experienced a clear warming trend, rapid population growth, and urbanization. The annual mean surface air temperature over China has increased by more than 1 °C, accompanied by more frequent and hotter summer days^{19–21}. The evident warming trend and more frequent heatwaves can reduce soil moisture and further affect crops, vegetation and water consumption, leading to detrimental impacts on food security and water resource sustainability in

China^{22,23}. Meanwhile, the intensity of hot extremes is projected to increase in the future due to the increased concentration of global greenhouse gases²⁴. However, studies on heatwaves and their changing behavior in China focus primarily on the increasing trends associated with anthropogenic effects (e.g., greenhouse gas warming, urban heat islands) and isolated drivers at a regional scale^{9,25–28}. A recent study revealed abrupt (i.e., sudden) intensification of country-averaged heatwave magnitude over China around 1996–1997 and alluded the changes to the increased global temperature²⁹. Systematic assessment of the abrupt intensification of heatwave in different geographic regions of China, however, has not yet been done. While large-scale climate anomalies associated with ENSO, AMO, and IOD have been suggested to affect the frequency, duration, and intensity of heatwaves in some areas of China^{11,20,29}, their relative contributions to the abrupt intensification in different regions and the underlying mechanisms remain unclear.

Here, we systematically assess the changing behaviors of summertime (June–August) heatwave intensity and test its robustness and regionality in China, using reliable meteorological observations (available from 1961 to 2017) with statistical techniques. Then we explore the non-stationary impacts of the dominant climate modes on heatwave intensity using a Bayesian dynamic linear model (DLM). To help understand the relevant mechanisms, we analyze atmospheric reanalysis data and perform model experiments using an atmospheric general circulation model (AGCM). This understanding is crucial for decadal

¹The National Key Laboratory of Water Disaster Prevention, Hohai University, Nanjing, China. ²College of Hydrology and Water Resources, Hohai University, Nanjing, China.

³Department of Atmospheric and Oceanic Sciences, University of Colorado Boulder, UCB 311, Boulder, CO, USA. ⁴Cooperative Innovation Center for Water Safety and Hydro Science, Hohai University, Nanjing, China. ⁵Key Laboratory of Water Big Data Technology of Ministry of Water Resources, Hohai University, Nanjing, China. ⁶State Key Laboratory of Tropical Oceanography, South China Sea Institute of Oceanology, Chinese Academy of Sciences, Guangzhou, China. ⁷Global Ocean and Climate Research Center, South China Sea Institute of Oceanology, Guangzhou, China. ⁸Department of Civil, Environmental, and Architectural Engineering, University of Colorado Boulder, Boulder, CO, USA.

✉email: wangweiguang@hhu.edu.cn

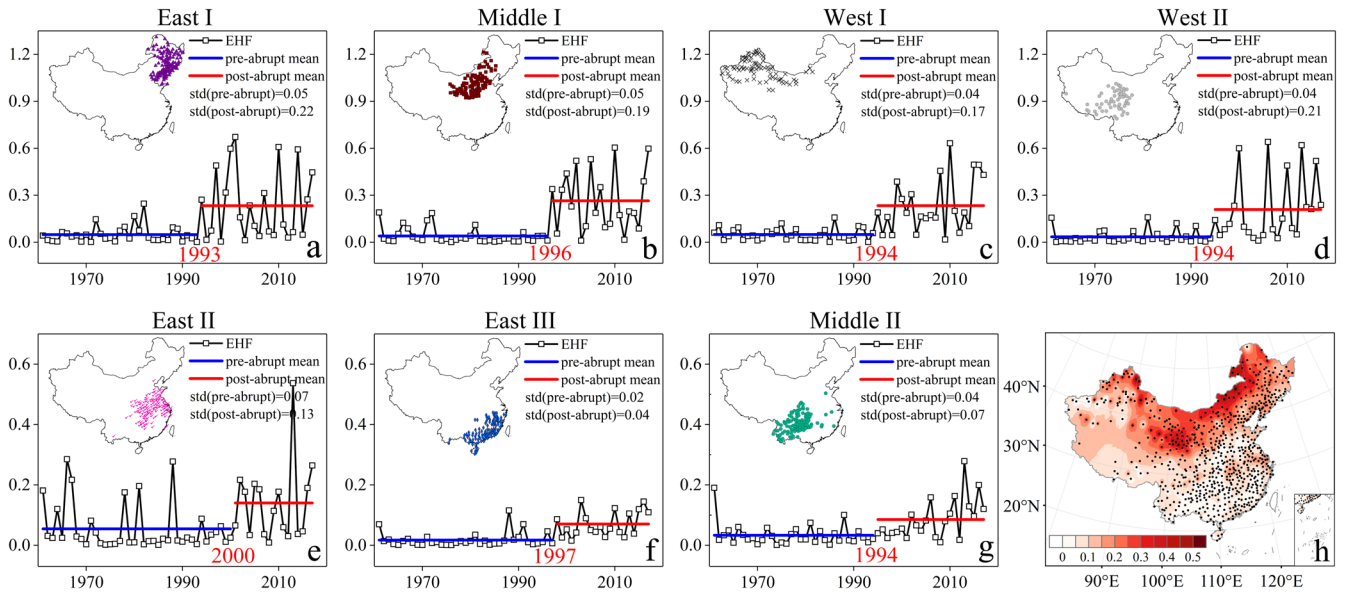


Fig. 1 Temporal variations of heatwave intensity. Time series of June, July and August (JJA)-mean excess heat factor (EHF) in 7 subregions (black line with squares) from 1961 to 2017 (a–g). The mean EHF values during the pre-abrupt and post-abrupt periods are shown in blue and red lines, and the year of abrupt change is denoted in red for each panel. The spatial distribution of EHF differences between the post-abrupt and pre-abrupt periods is shown in (h).

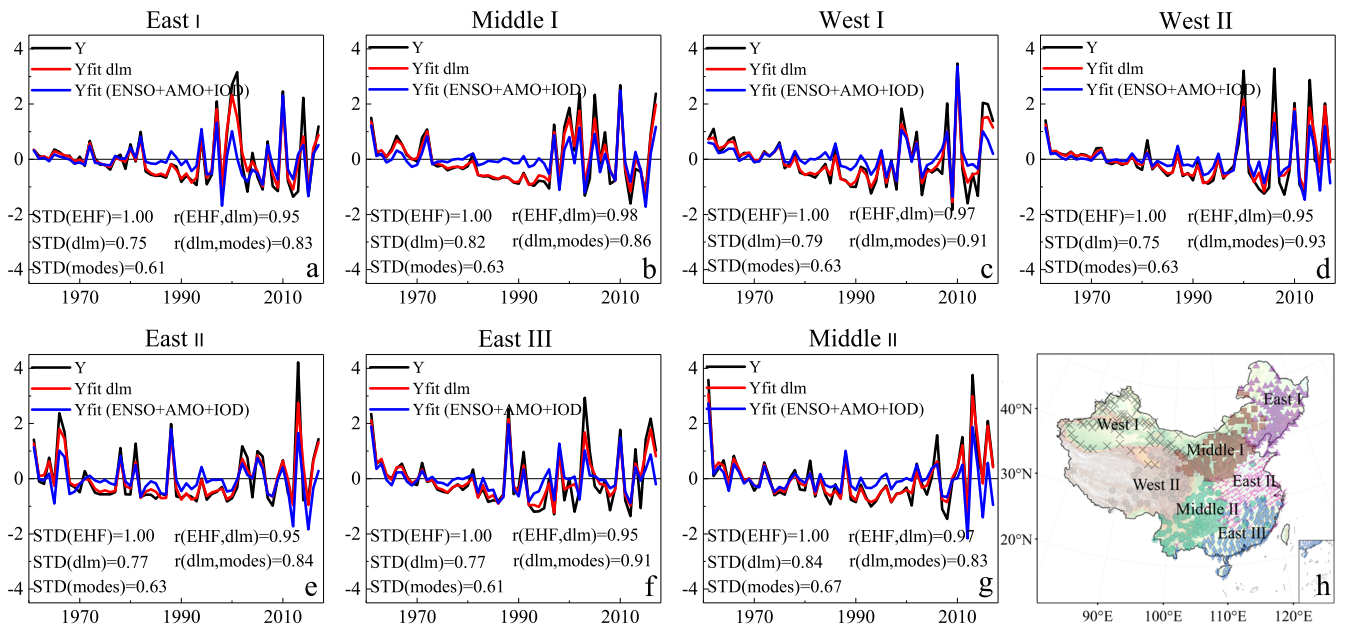


Fig. 2 Bayesian simulation of heatwave intensity. Time series of observed normalized JJA-mean heatwave intensity (Y , black line) from 1961 to 2017 (a–g), its Bayesian dynamic linear model (DLM) simulation ($Y_{fit} \text{ dlm}$, red line), and the total effects of all three climate modes (blue line; see section “Impacts of climate modes”). The standard deviation (STD) for each curve and the correlations between three climate modes are shown. The right bottom panel denotes the location of subregions (h).

predictions and near-term projections of heatwaves in different regions over China. The effective simulation of non-stationary impacts of climate modes and predictive ability presented by Bayesian DLM can improve the hindcast skill by over 10% and reduce the mean square error by more than 25% compared to conventional linear regression model³⁰, leading to a better forecast for the heat disasters than using a conventional linear model.

RESULTS

Abrupt changes of heatwaves

Using the Fuzzy C-Means algorithm, we identify seven distinct regions of heatwave variability over China (Fig. 1 and Supplementary Fig. 1). The three regions in northern China (East I, Middle I, and West I) and one region in western China (West II; Fig. 1a–d) have experienced greater increases in heatwave intensity than the rest three regions in southeast China (Fig. 1e–g). The abrupt

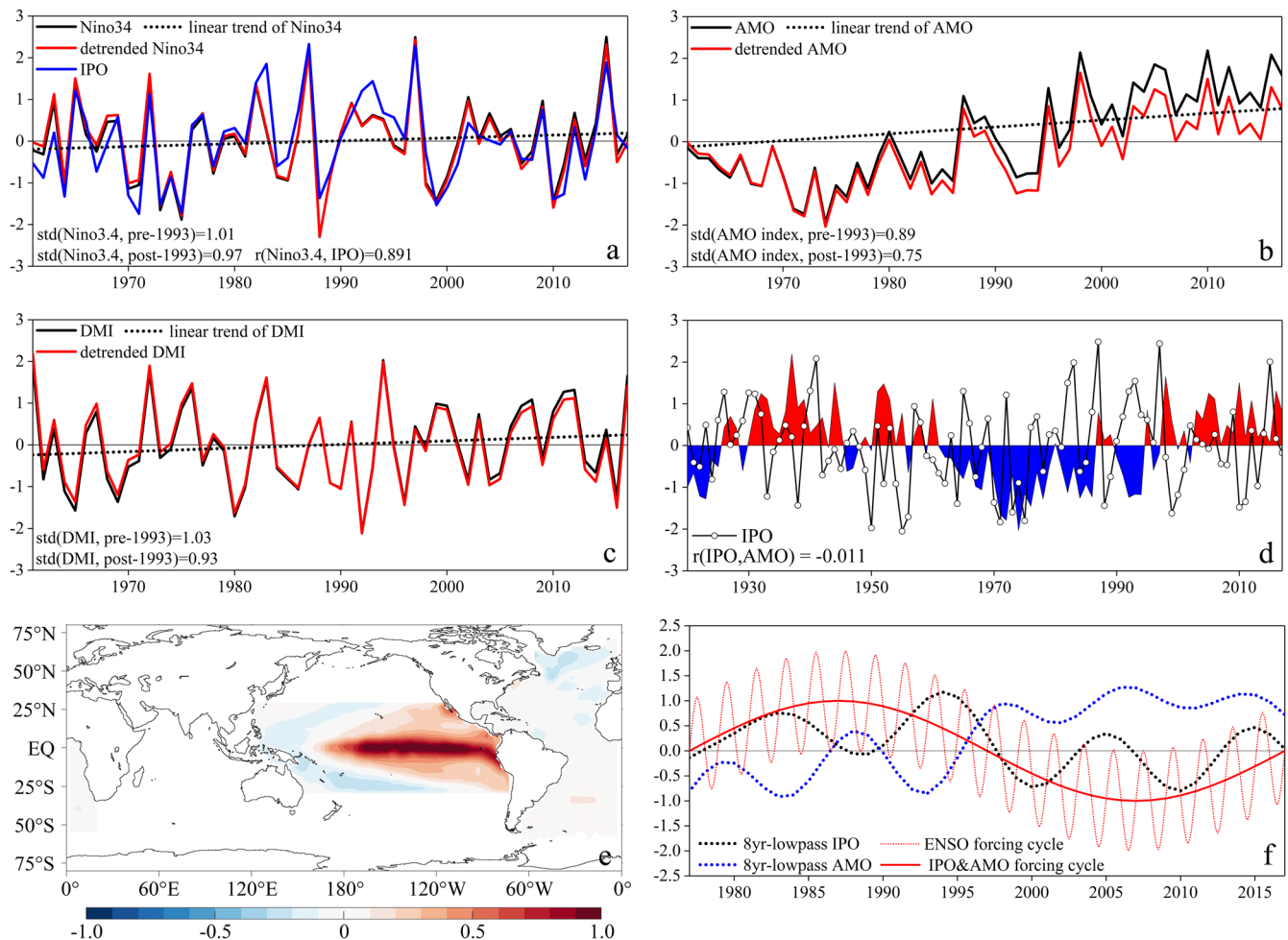


Fig. 3 Time series of JJA-mean normalized climate mode indices based on monthly observational data with the 1961–2017 mean removed. **a** Nino3.4 index; **b** the Atlantic multidecadal oscillation (AMO) index; **c** the Indian Ocean Dipole Mode Index (DMI); **d** the detrended IPO index (black line) and AMO index (shading) from 1920 to 2017. **e** Spatial patterns of SST anomalies (SSTA; °C) associated with a positive IPO over the Pacific and negative AMO over the North Atlantic (color shading); **f** time series of 8 yr-lowpass-filtered normalized IPO and AMO indices (black and blue dotted curves), an idealized sinusoidal SSTA that mimics the IPO index (thick solid red) and AMO index but with an opposite sign, and a sinusoidal SSTA with a 2-year period representing ENSO interannual variability (thin solid red).

changes exceed 95% significance level in East I, Middle I, West I and West II regions as well as East II area in both Pettitt and moving t -tests; however, the rest two southern regions (East III and Middle II) have inconsistent results from the two different methods (Supplementary Fig. 2 and Table 1). The mean heatwave intensities for the post-abrupt change period are 4.8, 6.7, 4.8, and 6.1 times of those of the pre-abrupt period in East I, Middle I, West I, West II regions, respectively, and the heatwave variability—measured by the standard deviation (STD) of EHF—also exhibits evident enhancement in each region. The strong intensifications of heatwave magnitudes, as shown by the difference between the EHF averaged for the post- and pre-abrupt period at each observational station, are also clearly seen in regions of northern and western China (Fig. 1h). The increased variability amplitude demonstrates that individual heatwave events become more intense.

For comparison, the daily-mean air temperatures from NCEP/NCAR and ERA5 reanalysis products are also used to calculate EHF (Supplementary Fig. 3). The heatwave intensities averaged over China from observations, NCEP/NCAR reanalysis and ERA5 reanalysis datasets show consistent abrupt changes in 1996 as tested by both Pettitt and moving t methods, although the reanalysis datasets show smaller increase in EHF magnitudes than the observations from meteorological stations. The abrupt EHF

increases in ERA5 reanalysis agree well with that of station data across China except for the Tibet plateau area where only a few meteorological stations are available (Fig. 1 and Supplementary Fig. 3). By contrast, NCEP/NCAR reanalysis data show reasonable EHF increase only in northeast China (top row of Supplementary Fig. 3). Therefore, we will use ERA5 data for further calculations hereafter. After removing the linear trend, the abrupt increase in heatwave intensity remains evident for the four northern and western areas, although the magnitudes are reduced (Fig. 2a–d, black lines; Supplementary Table 2). This result suggests that the warming trend—which is attributed primarily to global warming by previous studies—indeed enhances heatwave amplitudes across China, but it cannot explain the strong and abrupt EHF intensity increase (both mean and variability) especially in northern and western China.

Impacts of climate modes

The impacts of the three dominant climate modes—ENSO, AMO, and IOD—affecting Asia's climate are examined. Using the JJA-mean detrended indices of ENSO, AMO, and IOD as predictors and detrended heatwave intensity (EHF) as the predictand, the Bayesian DLM can simulate the observed interannual and longer timescale variability of heatwave intensity in all regions, including

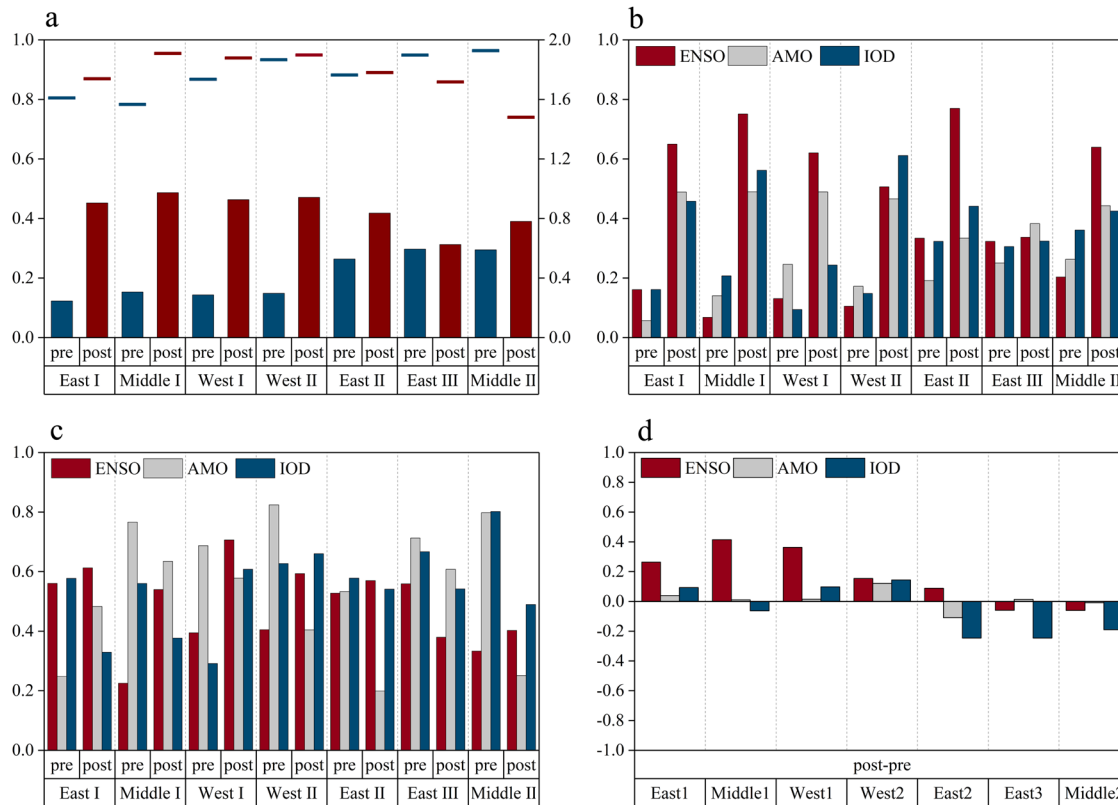


Fig. 4 Contribution of climate modes to heatwave intensity in Bayesian DLM for the pre-abrupt and post-abrupt periods in each of the seven subregions. **a** The correlation coefficient between the total climate modes' contribution (ENSO + AMO + IOD) and the full Bayesian DLM simulations (horizontal segments, left axis), and the standard deviation (STD) of total climate modes' contribution for the pre-abrupt and post-abrupt periods (histogram, right axis) for each region. **b** The STD of heatwave intensity is explained by ENSO, AMO, and IOD, respectively. **c** The correlation between DLM simulation and each climate mode's contribution. **d** The difference of EHF between pre-abrupt and post-abrupt periods (post subtracts pre) contributed by each climate mode.

their magnitudes and abrupt intensity increases (Fig. 2, compare black and red lines). The three climate modes together explain most of the model-data correlation and observed variances (Fig. 2, blue lines). During the post-abrupt period, the combined impacts of ENSO, AMO, and IOD explain 62.35%, 70.01%, 66.20%, and 63.64% (STD_{modes}/STD_{EHF}) of the observed heatwave intensification in East I, Middle I, West I, and West II regions, respectively. For the Bayesian DLM simulations, the combined impacts of total climate modes can contribute 85.56%, 89.33%, 86.72%, and 88.11% (STD_{modes}/STD_{dlim}) to the simulations for the four regions. There is however a portion of EHF that cannot be explained by these climate modes, suggesting that other factors (e.g., atmospheric internal variability) can also contribute to heatwave activities. Note that the amplitudes of ENSO, AMO, and IOD indices are similar for the pre- and post-abrupt change periods (Fig. 3a–c), suggesting that the modeled abrupt increases in heatwave intensity in the Bayesian DLM (Fig. 4a) arise from their significantly intensified coefficients (Supplementary Fig. 4) rather than from variations of climate modes' strength. Physically, these results suggest that for the same strength of a climate mode, its impacts are more effective and larger during the post-abrupt period. Relevant physical causes are discussed below.

The impacts of climate modes have substantial increases during the post-abrupt period, as can be seen from both the increased STD of climate modes' contribution and its correlation with total DLM simulation in the four regions of northern and western China (East I, Middle I, West I, and West II) although the correlation increased little in West II (Fig. 4a). Therefore, we focus on these four northern and western China regions hereafter. ENSO accounts for the largest fraction of heatwave intensification in all four

regions and dominates the combined effect of IOD and AMO in East I, Middle I, and West I (Fig. 4b, d). While the AMO impact is weak or negligible in these three regions, the IOD impact is larger and non-negligible in East I and West I. In West II area, ENSO, IOD, and AMO have comparable effects on the enhanced EHF (Fig. 4d). The effect of ENSO is weak overall before the 1990s, but after the year of abrupt change, the DLM coefficient of ENSO becomes strongly negative and exceeds the 95% confidence interval of the constant coefficient of the conventional linear regression model in each region (Supplementary Fig. 4a–d). The negative coefficient suggests that the negative phase of ENSO (IPO), which corresponds to La Niña (negative IPO), enhances the heatwave intensity during the post-abrupt period.

The impacts of AMO and IOD, especially AMO, are more complex. For instance, during the pre-abrupt change period, the AMO is in a negative phase overall with significant interannual variability (Fig. 3b, d), and its impacts on heatwave intensity—measured by its DLM coefficients (Supplementary Fig. 4e–h)—are weak in all four regions. During the post-abrupt change period, the AMO is in a positive phase (Fig. 3b, d); its impacts on heatwaves (DLM coefficient), however, change from negative before ~2008 to positive thereafter, indicating its non-stationary relationship with heatwave intensity. Physically, this suggests that the sea surface temperature anomalies (SSTAs) associated with the AMO might have experienced a pattern change around 2008, resulting in different impacts on China's climate. Indeed, the AMO index—the averaged SSTA in the North Atlantic Ocean—is associated with significantly different SSTA patterns before and after 2008 (Supplementary Fig. 5). For the IOD, its impacts enhance during the post-abrupt period with negative IOD

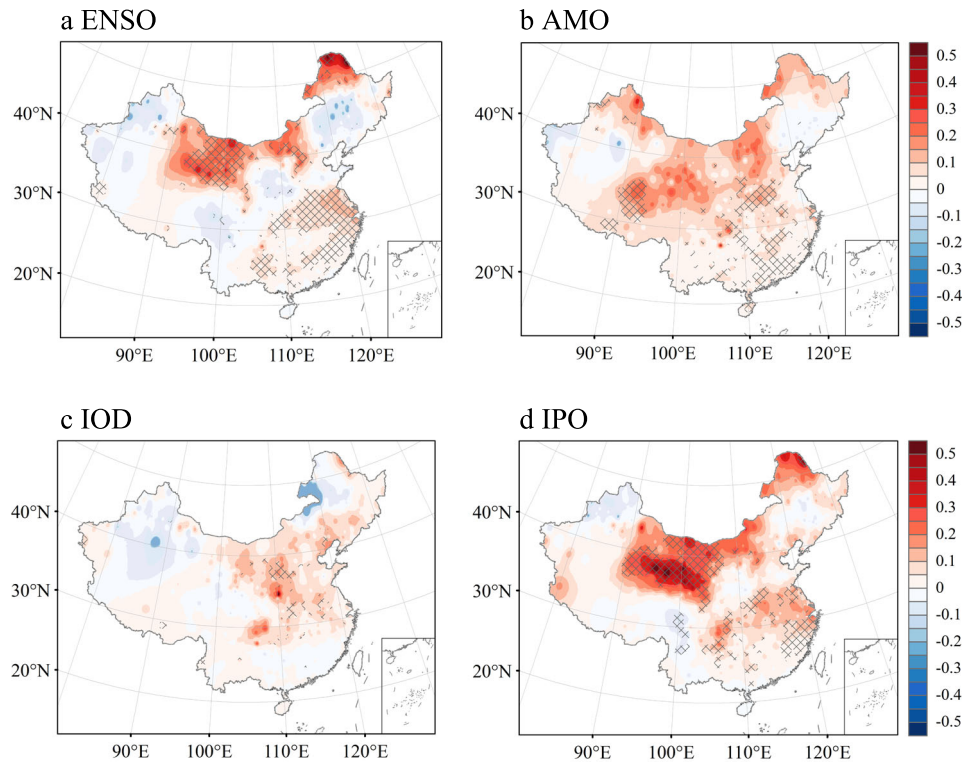


Fig. 5 Composite maps of heatwave intensity (JJA-mean EHF) changes associated with phase changes of observational climate modes indices with trend removed for the 1961–2017 period. Hatching indicates statistical significance according to the standard *t*-test at the 90% confidence level. **a** La Niña minus El Niño; **b** positive minus negative phases of AMO; **c** positive minus negative phases of IOD; and **d** negative minus positive phases of IPO.

enhancing the heatwaves as shown by its negative DLM coefficient (Supplementary Fig. 4i–l). Note that the DLM coefficient of IOD in the West II area changes sign during the post-abrupt period, from positive before ~2007 to negative thereafter. We further perform partial Bayesian DLM to investigate whether this changing sign of the IOD coefficient is artificial. Compared to the Bayesian DLM using all three climate modes, the DLM coefficients of IOD in partial Bayesian DLM also change the sign from positive before ~2007 to negative albeit with a smaller amplitude (Supplementary Fig. 6). The reason for this change in the West II Tibet area is unclear and could be related to the relatively sparse meteorological stations in the region, atmospheric internal variability or other forcings on the EHF over the Tibet Plateau.

While our discussions above are based on Eq. (14) with multiple predictors, we have also examined each climate mode's impact with a single predictor (e.g., ENSO index) in the Bayesian DLM. Then assess the impact of other climate modes using partial Bayesian DLM, with AMO index and DMI as the predictors and the EHF residual (with ENSO effect removed) as the predictand (Supplementary Figs. 7, 8). The dynamic coefficients of individual predictors show similar variations with the results of multi-predictors (compared with Supplementary Fig. 4). For example, the DLM coefficient of ENSO with a single predictor is negative, indicating that La Niña (negative IPO) acts to intensify heatwaves. This result is consistent with the ENSO impact of the multi-predictors simulation. Likewise, the results of the AMO and IOD impacts are also consistent with those of multi-predictor simulations (Supplementary Figs. 9, 10).

To reveal the spatial patterns of heatwave intensity changes associated with phase changes of the climate modes, we perform composite analysis for the EHF using the climate indices (Fig. 5). Consistent with our discussions above, La Niña and the negative phase of IPO indeed enhance heatwaves, especially in northern regions of China relative to their positive phases. For the positive

phase of AMO and IOD, heatwaves intensify across China with the largest enhancement occurring in northern China relative to their negative phases, and the heatwaves show the smallest increase during positive phases of IOD. Note that Fig. 5 shows the EHF differences between the two phases of each climate mode, rather than the contributions of climate modes to the abrupt heatwave intensification since the 1990s.

Relevant physical processes for the abrupt intensification of heatwaves

In this subsection, we will first analyze the reanalysis product together with the meteorological station data, to demonstrate that the enhanced high-pressure system over the Eurasian continent plays an important role in generating the warmer surface air temperature and intensified heatwave (i.e., EHF) during the post-abrupt period. Then we discuss the effects of climate modes on the Eurasian high and heatwave intensification. Finally, we hypothesize that atmospheric circulation anomalies associated with the concurrence of interdecadal phase transitions of the IPO and AMO during the 1990s increase surface air temperature and enhance the heatwave magnitudes induced by atmosphere internal variability and ENSO. We test this hypothesis by performing AGCM experiments.

Compared to the pre-abrupt period, both sea level pressure and 500 hPa geopotential height have increased throughout China, especially over the Eurasia that spans northern and western China (Fig. 6b, c) where strong warming of surface air temperature and heatwave intensification are observed (Figs. 1h, 6a and Supplementary Fig. 3). A significant high-pressure system with a center located on the north side of Eurasia controls the mainland China (Fig. 6c). This result indicates that the warmer surface air temperature during the post-abrupt period yields stronger heatwaves.

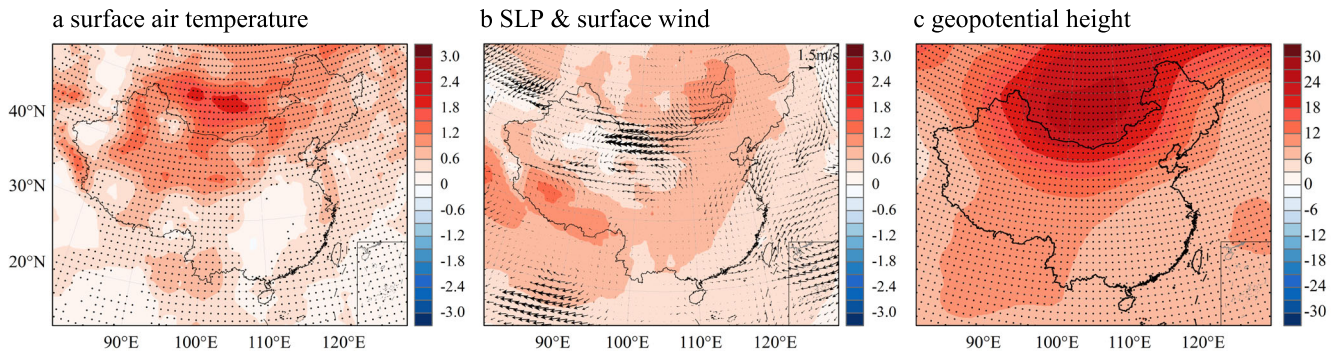


Fig. 6 The differences between the post-1996 period and the pre-1996 period (post subtracts pre) of JJA-mean maps from ERA5 reanalysis data. **a** Surface air temperature ($^{\circ}\text{C}$), **b** sea level pressure (hPa) and surface wind (m s^{-1}), **c** 500 hPa geopotential height (m). The black dots indicate the changes significant at the 90% confidence level.

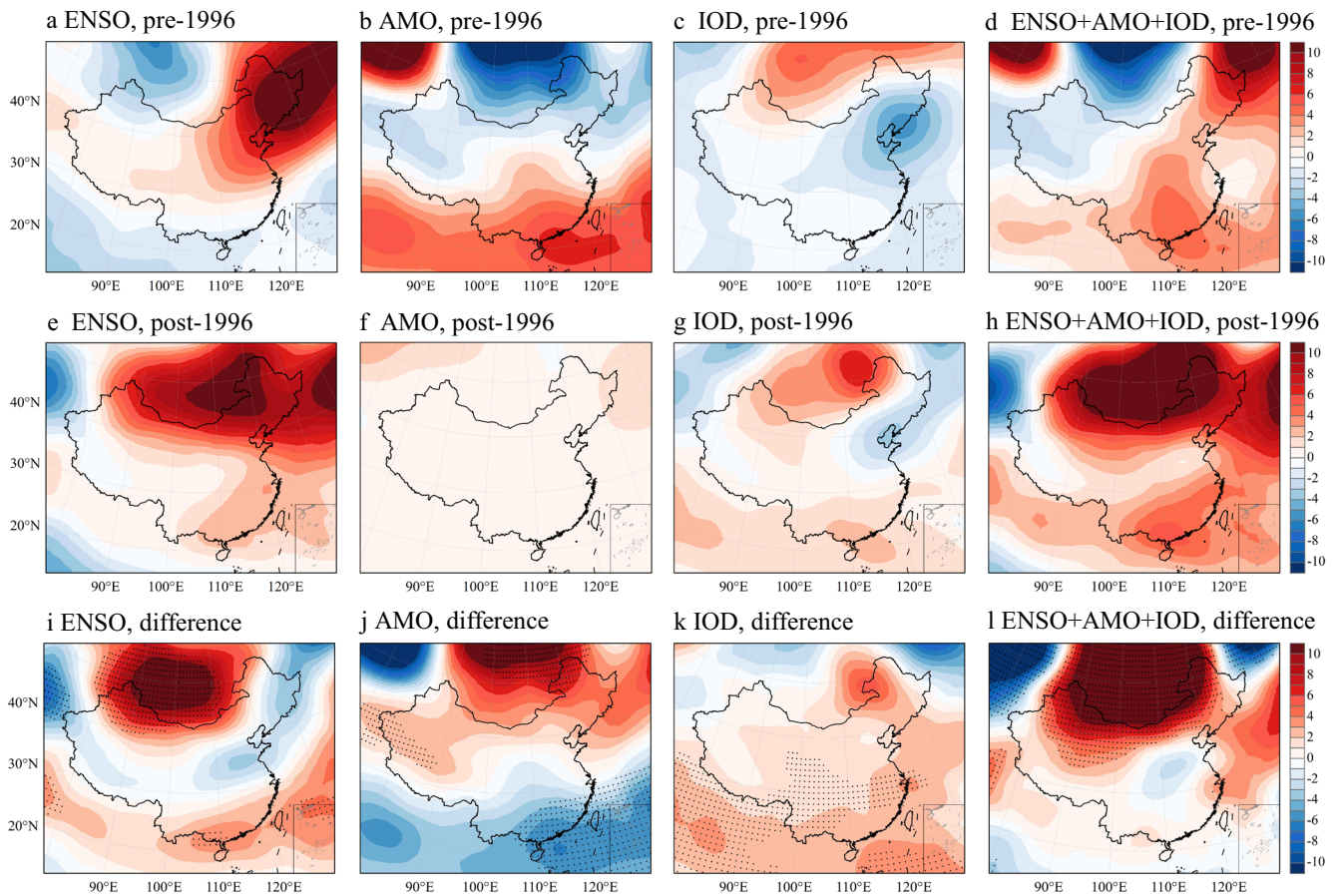


Fig. 7 The JJA-mean composite maps of 500 hPa geopotential height anomalies from Bayesian DLM simulation. **a–d** 500 hPa geopotential height contributed by ENSO, AMO, IOD, and the sum of three climate modes averaged for the pre-1996 period (1961–1996); **e–h** Same as (**a–d**) but for the post-1996 period (1997–2017); **i–l** Same as (**a–d**) but for the differences between pre-1996 and post-1996 periods (post subtracts pre). The black dots indicate the changes significant at 90% confidence level.

The increased 500 hPa geopotential height and sea level pressure (Fig. 6b, c) cause anomalous atmosphere subsidence and therefore reduce cloud cover (Supplementary Figs. 11a, 12a). The enhanced sinking motion contributes to the surface warming via adiabatic heating (Supplementary Fig. 11b), and the reduced cloud cover increases downward solar shortwave radiation which warms the earth's surface, especially in northeast China (Supplementary Fig. 12c). In the central and western parts of northern China, reduced latent heat loss from surface to the atmosphere (Supplementary Fig. 12e), which corresponds to reduced evaporative cooling at the surface, and reduced outgoing longwave

radiation (Supplementary Fig. 12f) warm up Earth's surface. The warmer ground heats up the surface air by increasing upward sensible heat flux (Supplementary Fig. 12d). In addition to surface heat fluxes, horizontal advection has significant contributions to the warm surface air temperature in West II (Supplementary Fig. 13).

The fundamental dynamics for ENSO and AMO to affect China's climate through Gill-type response and atmospheric Rossby waves have been discussed in existing studies^{31–33}. Located in the East Asian monsoon region, the climatic condition in China is sensitive to SSTAs since they can drive persistent anticyclones and

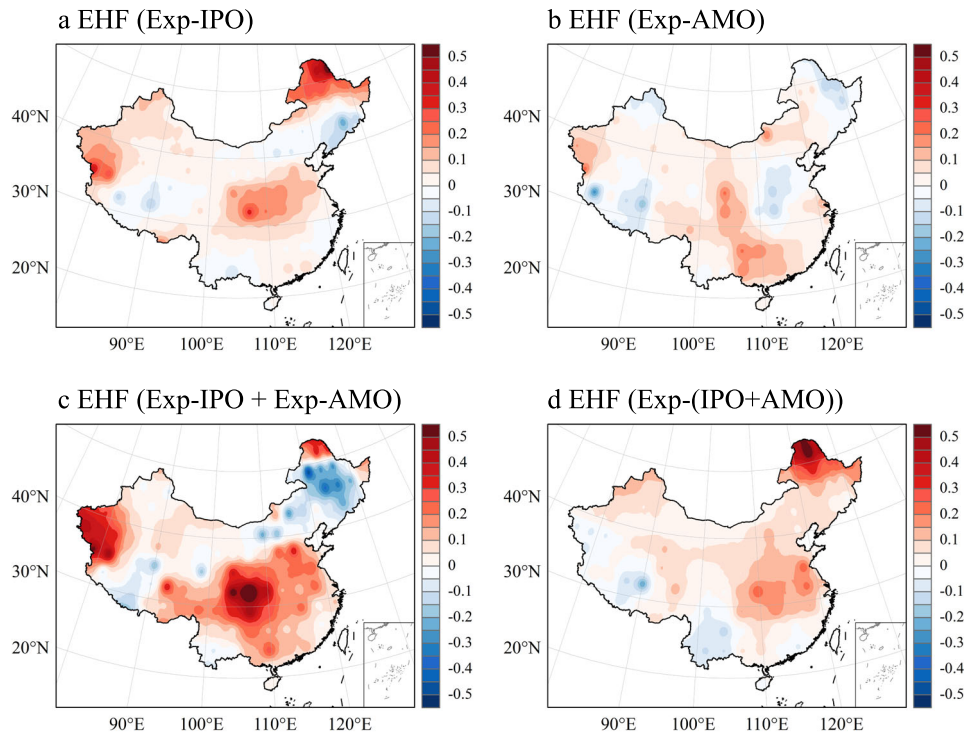


Fig. 8 Changes of JJA-mean heatwave intensity measured by EHF from the AGCM experiments. The differences between the last 20-year mean and the first 20-year mean results. **a** EHF from Exp-IPO; **b** EHF from Exp-AMO; **c** EHF calculated by daily TS from Exp-IPO+Exp-AMO; and **d** EHF from Exp-(IPO+AMO).

modulate the associated dynamics^{34,35}. The Bayesian DLM simulates the strong changes of 500 hPa geopotential height between the post- and pre-abrupt periods over China (Fig. 7), with STD ratios between the DLM simulated and ERA5 observed values >0.86 and correlation coefficients exceeding 0.97 over China (Supplementary Fig. 14). The three climate modes together can explain a large fraction of geopotential height enhancement over northern China. The ENSO contribution is centered in Eurasia similar to the observed change. The AMO contribution shows weaker magnitude but it is significant in western areas, while the IOD contribution is positively centered in East I.

During the 1990s, the IPO (i.e., ENSO decadal variability; Fig. 3a) transits from a positive to negative phase and the AMO changes from negative to positive (Fig. 3f). The change in decadal IOD variability is weak compared to that of the IPO and AMO (Fig. 3f and Supplementary Fig. 15). Because negative IPO and positive AMO generally tend to enhance heatwaves (Fig. 5) based on the negative regression coefficient of IPO and positive coefficient of AMO (dashed black lines of Supplementary Fig. 4), we hypothesize that the combined effects of the IPO negative phase transition and AMO positive phase transition around the mid-1990s cause atmospheric circulation anomalies, warm the surface air and enhance the heatwave magnitudes, resulting in the intensification of heatwaves in China. This also helps explain the enhanced magnitude of the ENSO coefficient in the Bayesian DLM (Supplementary Fig. 4). It is also possible that ENSO, the dominant mode for heatwave intensification, has experienced SSTA pattern change due to ENSO diversity (i.e., Central Pacific ENSO versus Eastern Pacific ENSO), and the SSTA pattern in the recent two decades causes stronger heatwaves. The occurrences of the two types of El Niño events, however, have similar chances between the 1980–1996 and 1996–2017 periods (Table 1 of Zhang and Han³⁶), and thus are not likely the cause for the abrupt heatwave intensification.

To test our hypothesis, we perform three AGCM experiments using ECHAM4.6 to assess the impacts of the IPO, the AMO, the

ENSO, the combined IPO and AMO, and the combination of all three modes. A total of four AGCM experiments are performed: Exp-IPO, Exp-AMO, Exp-(IPO+AMO), and Exp-(IPO+AMO+ENSO), which assess the impacts of IPO, AMO, combined IPO with AMO, and combined IPO, AMO, and ENSO. The spatial patterns of the SSTAs associated with each climate mode are obtained by regressing SSTA on the normalized climate mode indices and then are multiplied by a sinusoidal wave with a 40-year period to represent the observed inter-decadal changes of IPO and AMO (Fig. 3f). The effect of ENSO represents interannual SST variability with an idealized 2-year period, which is superimposed on the interdecadal SSTAs of AMO and IPO that force Exp-(IPO+AMO) (Fig. 3f). The control (CTRL) experiment is forced by the climatological SST. Thus, the impacts of IPO, AMO, IPO+AMO, and IPO+AMO+ENSO on the heatwaves can be quantified by comparing the corresponding results with the CTRL experiment. Note that in these experiments, the IPO and AMO effects are only at an interdecadal timescale, and ENSO is only at an interannual timescale with an idealized 2-year cycle (see Fig. 3f for their idealized indices).

First, we analyze the magnitudes of heatwave changes by calculating EHF difference between the post- and pre-abrupt change period using daily results from Exp-IPO, Exp-AMO, and Exp-(IPO+AMO) (Fig. 8). Exp-IPO shows that the IPO alone enhances heatwaves in central, northeastern and western China, and AMO alone (Exp-AMO) weakly enhances heatwave intensity across southern China. Their combined impacts from Exp-(IPO+AMO), however, show evident increases in heatwave intensity in most regions of northern China (Fig. 8d) where abrupt heatwave intensification is observed. The linear superposition of their impacts, Exp-IPO+Exp-AMO (Fig. 8c), however, cannot produce the strong heatwave intensification in northeast China, suggesting that nonlinear interactions between the IPO and AMO effects, which are included in Exp-(IPO+AMO), play an important role. The time series of JJA-mean EHF calculated from Exp-(IPO+AMO) in each of the four regions of northern and west China also show

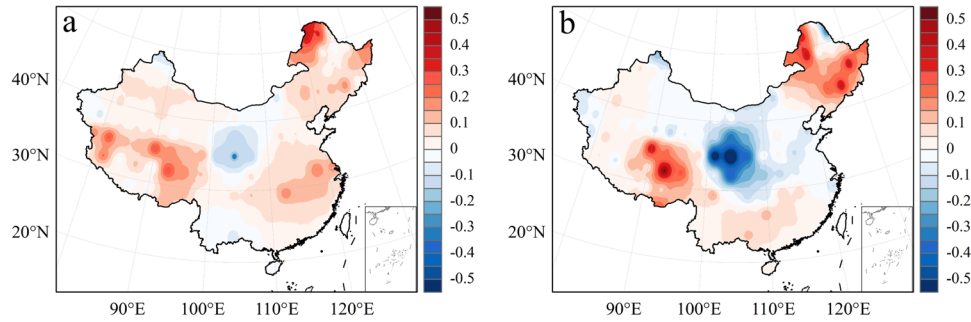


Fig. 9 Changes of JJA-mean heatwave intensity measured by EHF from the AGCM experiment Exp-(IPO+AMO+ENSO). **a** The differences between the last 20-year mean and the first 20-year mean results. **b** The differences in the composites of La Niña episodes between the last 20-year and first 20-year periods.

heatwave intensification during the post-abrupt change period (Supplementary Fig. 16). Since only interdecadal SSTAs of the IPO and AMO are used to force the AGCM, the enhanced amplitude of interannual EHF in Exp-(IPO+AMO) results mainly from the interdecadal modulation of atmospheric internal variability by IPO and AMO.

The above AGCM experiments demonstrate that the interdecadal SSTAs associated with the concurrent phase transitions of the IPO (positive to negative) and AMO (negative to positive) around the mid-1990s indeed cause heatwave intensification. Given that the impact of ENSO on EHF is intensified during the post-abrupt period, we expect that the combined IPO and AMO interdecadal phase transitions may also enhance ENSO's interannual impacts on heatwave amplitude. To test this hypothesis, we analyze the results from Exp-(IPO+AMO+ENSO) (Fig. 9 and Supplementary Fig. 17). The composites differences of La Niña episodes between the post- and pre-abrupt periods, which isolate ENSO impacts and damp the effects of atmospheric internal variability, show that the same amplitude La Niña events indeed produce stronger heatwaves during the post-abrupt period in the East I and West II regions. Even though the AGCM results contain model errors, the good agreements between our idealized AGCM results and observational analyses prove that the concurrent interdecadal phase transitions of the IPO and AMO explain a major portion of the abrupt increase of heatwave intensity around the mid-1990s, by modulating atmospheric internal variability and interannual ENSO's effects.

DISCUSSION

The strong societal and ecosystem impacts of heatwaves emphasize the urgency for an improved understanding of their driving mechanisms and changing behavior on decadal and longer time scales in a warming climate. Using meteorological station observations and reanalysis datasets, we detect robust intensification of heatwave magnitudes over China in the past two decades, with an abrupt increase in heatwave intensity around the mid-1990s in northern and western China (East I, Middle I, West I, and West II regions of Fig. 1). The intensification remains robust in northern and western China after we remove the multidecadal linear trend of heatwave intensity, which has been attributed to anthropogenic warming by previous studies (Fig. 2). By performing Bayesian DLM and AGCM experiments, we show that the enhanced impacts of major climate modes (ENSO, AMO and IOD) during the post-abrupt period explain a major portion of the abrupt heatwave intensification. Despite the climate mode indices do not show increased amplitudes (Fig. 3), their impacts on heatwave intensity intensified as shown by their larger Bayesian DLM coefficients (Supplementary Fig. 4). Physically, this means that climate modes generate favorable atmospheric conditions for strong heatwaves to occur in northern and western China during

the past two decades, which further amplify the already enhanced heatwaves due to anthropogenic warming.

During the post-abrupt change period, the enhanced Eurasian high-pressure system causes anomalous atmosphere subsidence, which contributes to Earth's surface warming in northern China via adiabatic heating, increased downward solar shortwave radiation due to reducing cloud cover, and weakened latent heat loss. The warm ground heats up surface air through sensible heat flux, and advection also contributes to the warm surface air in the West II region. The concurrent interdecadal phase transitions of the IPO (from positive to negative) and the AMO (from negative to positive) around the mid-1990s are the main cause for the observed intensified Eurasian high-pressure system, which warms the surface air and results in the abrupt intensification of heatwaves around the mid-1990s. Our AGCM experiments show that the interdecadal SSTAs associated with the IPO and AMO enhance the year-to-year heatwave magnitudes by modulating atmospheric internal variability and interannual climate modes (e.g., ENSO). The nonlinearity of the atmospheric system affects the IPO and AMO impacts and is important in some regions. Further investigation is needed to understand the sources of atmospheric internal variability and their interplay with climate modes, and this is an area of our future research.

Our results indicate that the concurrences of interdecadal phase transitions of the IPO and AMO can aggravate the intensified heatwaves due to anthropogenic warming in some decades but weaken them during other decades, causing abrupt changes in heatwave intensity in different regions of China and other countries. Continued greenhouse gas warming is altering the background climatic conditions and likely the dynamics governing these climate modes³⁷. The warming ocean temperatures may also amplify the impacts of climate modes on the ecosystems and extreme events (e.g.³⁸). Thus, it is imperative to understand the climate modes' influences and their interplay with the changing climate. This understanding may help improve decadal predictions and near-term projections of climate and extreme events and therefore contribute to informed decision-making.

METHODS

Data

Daily maximum and minimum temperatures of meteorological stations from 1961 to 2017 were obtained from China Meteorological Administration and were quality controlled based on a national standard quality management system. The total 718 meteorological stations used in this study are shown in Fig. 1h and Supplementary Fig. 1. In this study, the three dominant climate modes—ENSO, AMO, and IOD—affecting Asia climate are examined, which are represented by monthly Niño3.4 index, AMO index, and DMI from June to August, respectively^{39–41}. The

Interdecadal Pacific Oscillation (IPO) index⁴² is also analyzed and compared with the ENSO index (Fig. 3a); their JJA-mean indices are highly correlated with a correlation of 0.89 for the 1961–2017 period and 0.78 for their decadal components (8 yr low-passed filtered values). The high correlations between IPO, Pacific Decadal Oscillation, and ENSO decadal variability have been shown by previous studies, with correlation coefficients being 0.89 for the past century^{43,44}. Therefore, hereafter we use the IPO and decadal variability of ENSO interchangeably and use the IPO index to estimate the impact of ENSO decadal variability on the abrupt change of heatwave intensity. The JJA-mean index of each climate mode is calculated by averaging June, July, and August values, with the monthly climatology of 1961–2017 removed. In addition, monthly global SST from the NOAA Extended Reconstructed SST V5⁴⁵ is used to conduct the regression analysis.

For comparison, daily-mean air temperatures from ERA5 and NCEP/NCAR reanalysis products^{46,47} are also used to calculate heatwave intensity. To help understand the relevant physical mechanisms, we also analyze ERA5 reanalysis geopotential height, sea level pressure, surface zonal and meridional winds, vertical velocity, total cloud cover, and temperature advection. To assess the change of surface heat flux associated with heatwave intensification, the surface latent heat flux, sensible heat flux, shortwave radiation flux, and longwave radiation flux are also analyzed.

Definitions of heatwave, identification of homogeneous regions, and detection of abrupt change

Definitions of heatwave in existing literature are not consistent. The most commonly used definition is the relative threshold of 90th or 95th percentile daily temperature to evaluate the excessive heat days and nights in Europe, Australia, and India (e.g. refs. 48–50). Here, the EHF calculated with daily maximum and minimum surface air temperatures was selected because of two improvements compared to the common definition: One is the incorporation of day and night heat conditions; another is the consideration of local antecedent heat conditions. The local antecedent heat condition can enhance or weaken the heat amplitude for a given day^{51,52}. The EHF was proposed based on two concepts named excess heat and heat stress. This method has been intensively tested for reliably detecting heatwave events and more accurately representing heatwave intensity (e.g. refs. 53–56). To assess the temporal evolution of heatwave intensities in different regions over China, we calculate the excess heat factor (EHF) using daily maximum and minimum temperature data during summer (06/01–08/31) observed from meteorological stations for the period of 1961–2017. The excess heat expresses an unusually high-temperature condition with an average of maximum and minimum daily temperatures (T_{\max} and T_{\min}) further averaged over a three-day period and comparing it against a long-term temperature:

$$EHI_{\text{sig}} = (T_i + T_{i-1} + T_{i-2})/3 - T_{i95}, \quad (1)$$

where T_{i95} is the 95th percentile of daily mean temperature (T_i) for the entire period of 1961–2017. In our study, the T_{i95} is calculated for each day (i) with a 15-day window (from T_{i-7} to T_{i+7}) centered on T_i and at each station. The daily mean temperature is defined as:

$$T_i = (T_{\max} + T_{\min})/2, \quad (2)$$

where T_i is calculated from 1 June to 31 August during the period of 1961–2017.

The heat stress characterizes a heat anomaly from the acclimatization over the recent past with the average temperature

over a 3-day period compared against a short-term temperature:

$$EHI_{\text{accl}} = (T_i + T_{i-1} + T_{i-2})/3 - (T_{i-3} + \dots + T_{i-32})/30, \quad (3)$$

The EHF considers both EHI_{sig} and EHI_{accl} and is defined as

$$EHF = EHI_{\text{sig}} \times \max(1, EHI_{\text{accl}}), \quad (4)$$

which provides a more effective and comprehensive measurement of heatwave intensity.

We classify the regions using the Fuzzy C-Means algorithm, which is a commonly used clustering method (e.g. refs. 57,58). A finite dataset $X = \{x_1, x_2, x_3, \dots, x_n\}$ in a feature space R^s , is classified by FCM method into c clusters ($2 \leq c < n$). The cluster center is $V = \{v_1, v_2, v_3, \dots, v_n\}$. The membership matrix is

$$U = \{u_{ij}\} \quad (5)$$

where u_{ij} is the membership degree of the i th data to the j th cluster. In the FCM, u_{ij} should satisfy the following conditions:

$$u_{ij} \in [0, 1], \quad (6)$$

$$\sum_{i=1}^c u_{ij} = 1, \quad (7)$$

$$0 < \sum_{j=1}^n u_{ij} < 1. \quad (8)$$

The optimized objective function of FCM algorithm is

$$J(U, V) = \sum_{i=1}^c \sum_{j=1}^n u_{ij}^m d_{ij}^2, \quad (9)$$

$$d_{ij} = \|x_j - v_i\| = \left[\sum_{j=1}^n (x_{ij} - v_{ij})^2 \right]^{1/2}, \quad (10)$$

where m is a fuzzy weighted parameter.

The optimized clustering number is determined by validity indices. In this study, three widely used validity indices, namely the Fuzziness performance index (FPI)⁵⁹, partition index (PI)⁶⁰, and Extended Xie–Beni index (XB)⁶¹ are selected to find the optimal number of clusters:

$$FPI(c) = 1 - \frac{(\frac{c}{N} \sum_{i=1}^c \sum_{j=1}^N (u_{ij})^2 - 1)}{(c-1)}, \quad (11)$$

$$PI(c) = \sum_{i=1}^c \frac{\sum_{j=1}^N (u_{ij})^m \|x_j - v_i\|^2}{N_i \sum_{k=1}^c \|v_k - v_i\|^2}, \quad (12)$$

$$XB(c) = \frac{\sum_{i=1}^c \sum_{j=1}^N (u_{ij})^m \|x_j - v_i\|^2}{N \min_i, j \|v_k - v_i\|^2}. \quad (13)$$

The optimal cluster number is found when the validity indices become smaller and stable. Note that the values of all three validity indices become smaller and stable when the cluster number ≥ 7 (Supplementary Fig. 1a). Therefore, 7 subregions are classified (Supplementary Fig. 1b): three east regions (East I, East II, East III), two middle regions (Middle I, Middle II) and two west regions (West I, West II).

The EHF averaged for each subregion is used to characterize regional heatwave intensity variation. Using the Pettitt test⁶², we show abrupt increases in heatwave intensities in all seven regions (Fig. 1a–g and Supplementary Table 1). The years of abrupt changes vary regionally, ranging from 1993 in region East I to 2000 in East II. The abruptness of heatwave intensity increase is further tested and supported by the moving t -test (Supplementary Fig. 2), with the moving step of 10 years to detect abrupt change within the decadal time scale.

Bayesian dynamic linear model (DLM)

Given that ENSO and its decadal variability (i.e., IPO), AMO and IOD have prominent impacts on weather and climate over China^{20,29,31,32,63,64}, here we investigate their impacts on heatwave intensity using the Bayesian DLM⁶⁵. The Bayesian DLM has the advantage of capturing the nonstationary impacts (e.g., abrupt change) of climate modes compared to the conventional linear regression model. We first calculate the linear trends of the heatwave intensity index and climate mode indices for the 1961–2017 period and then remove them from both heatwave intensity and climate mode indices to eliminate the effects of global-scale warming associated with increased greenhouse gases²⁹. The longer period of 1920–2017 is used to calculate the AMO trend since the AMO has 60–80 yr periods and exhibits a positive phase transition during 1961–2017 (Fig. 3d, color shading).

The conventional multiple-linear regression model has been widely used to examine the relationship between the independent predictors (X_1, \dots, X_n) and predictand, Y . However, nonstationary relationships between Y and X_i in a real geophysical system especially under a warming climate cannot be captured by the conventional linear model, because of the constant regression coefficients (b_i ; see Eq. (15) below) during the examination period. The Bayesian DLM allows coefficients b_i to vary with time and thus can capture the time-varying impacts of predictors x_i on predictand Y within the temporal period examined.

$$Y(t) = b_0(t) + b_1(t)X_1(t) + \dots + b_M(t)X_M(t) + \varepsilon(t), \quad (14)$$

and

$$b_i(t) = b_i(t-1) + w_i(t), \quad (15)$$

where $\varepsilon(t) \sim N[0, V(t)]$ and $w_i(t) \sim N[0, W_i(t)]$ are independent white noises or errors, distributed normally with a mean of 0 and variances of $V(t)$ and $W_i(t)$.

With this advantage, the Bayesian DLM has been recently applied to investigating the nonstationary effects of climate modes on oceanic and atmospheric variables^{66,67}. In this study, we use ENSO, AMO, and IOD indices as predictors because of their prominent impacts on China's climate and heatwave intensity as predictand. Since the correlation coefficient between JJA-mean Niño3.4 index and DMI is 0.42 for the 1961–2017 period, whereas the Bayesian DLM requires predictors to be independent, partial DMI was calculated by removing the ENSO effect from the DMI before applying the Bayesian model. By doing so the underlying assumption of the procedure is that ENSO has a unidirectional influence on IOD. Therefore, ENSO (IOD) impacts might be somewhat overestimated (underestimated). Since the DMIs with and without ENSO-effect removed are highly correlated, with the correlation coefficient reaching 0.91 (Supplementary Fig. 18), the overestimation/underestimation effects are likely small.

To further ensure the independence of ENSO and IOD impacts and avoid the overfit by Bayesian DLM, we also apply the partial Bayesian DLM method⁶⁶ by using the residual EHF, $Y' = Y(t) - (b_1(t) \text{ENSO}(t) + b_2(t) \text{AMO}(t))$, as the predictand and partial DMI as the predictor. This yields, $Y' = b_0(t) + b_1(t) \text{IOD}(t) + \varepsilon(t)$. We compare the IOD effects and its DLM coefficient in the partial DLM with that from the original DLM from Eqs. (14) and (15) are mentioned above (Supplementary Fig. 6). The AMO is independent of ENSO ($r = 0.02$) and IOD ($r = 0.1$) during JJA and serves as an independent predictor.

AGCM experiments

To investigate the impact of inter-decadal climate variability associated with the IPO and AMO on the intensification of heatwaves over China, we perform AGCM experiments using ECHAM4.6⁶⁸ from Max Planck Institute in Hamburg. ECHAM4.6 has

been widely used to study atmospheric responses to large-scale sea surface temperature anomaly (SSTA) forcing in the tropics^{69–72}. Four experiments are performed: one control (CTRL) and three sensitivity experiments (Exp-IPO, Exp-AMO, and Exp-(IPO+AMO)). The CTRL is forced with the monthly climatological SST field. In Exp-IPO, the SSTA associated with the IPO over the tropical and subtropical Pacific is added to climatological SST; In Exp-AMO, the SSTA associated with the AMO over the North Atlantic is added to climatological SST; In Exp-(IPO+AMO), both the IPO and AMO SSTAs are added to the climatological SST. To obtain the SSTAs associated with the IPO (AMO), we first obtain their spatial patterns by regressing SSTA onto the normalized Niño3.4 (AMO) index (Fig. 3a, b, e), and then multiply the SSTA patterns by a sinusoidal wave with a 40-year period to represent the observed inter-decadal changes of the IPO and AMO (Fig. 3d, f). Further, one additional experiment including ENSO impacts is also performed (Exp-(IPO+AMO+ENSO)) to better understand the modulation of IPO on ENSO and their combined impacts on heatwave intensity.

For experiment CTRL, the model was integrated for 42 years. For Exp-IPO, Exp-AMO, and Exp-(IPO+AMO), respectively, the model is also integrated for 42 years, with the first two years forced by SST climatology as in CTRL but the subsequent 40 years forced by the sum of SST climatology and the corresponding SSTAs. The first 2 years are discarded in our analysis of all experiments given that it takes a couple of years for the model to reach its equilibrium state. A three-member ensemble is performed for each of the sensitivity experiments. The 40 yr mean of CTRL represents the effects of climatological SST forcing, and the three-member ensemble mean of each sensitivity experiment measures the impacts of the IPO, AMO, and IPO+AMO, respectively. The solution difference (Exp-IPO–CTRL) assesses the IPO impact, (Exp-AMO–CTRL) estimates the AMO impact, and (Exp-(IPO+AMO)–CTRL) measures the combined effects of IPO and AMO. Note that due to the nonlinearity of the climate system, the combined IPO and AMO effects obtained from (Exp-IPO–CTRL)+(Exp-AMO–CTRL) are different with that from (Exp-(IPO+AMO)–CTRL).

DATA AVAILABILITY

The observations of daily maximum and minimum temperatures are available at <http://data.cma.cn/en>. Monthly climate modes indices from the NOAA Physical Sciences Laboratory are available at <https://www.esrl.noaa.gov/psd>. The atmospheric circulation variables and surface heat budget variables from the ERA5 reanalysis products are available at <https://cds.climate.copernicus.eu/cdsapp#!/search?type=dataset&text=ERA5>. Monthly global SST of the NOAA Extended Reconstructed SST V5 is available at <https://www.esrl.noaa.gov/psd/data/gridded/data.noaa.ersst.v5.html>.

CODE AVAILABILITY

The scripts are available from https://github.com/WeiJ2022/heatwave_2023npj/tree/master.

Received: 29 December 2022; Accepted: 17 July 2023;

Published online: 24 July 2023

REFERENCES

- Easterling, D. R. et al. Climate extremes: observations, modeling, and impacts. *Science* **289**, 2068–2074 (2000).
- Ciais, P. et al. Europe-wide reduction in primary productivity caused by the heat and drought in 2003. *Nature* **437**, 529–533 (2005).
- Guo, Y. et al. Quantifying excess deaths related to heat waves under climate change scenarios: a multicountry time series modelling study. *PLoS Med.* **15**, e1002629 (2018).
- Hansen, J., Ruedy, R., Sato, M. & Lo, K. Global surface temperature change. *Rev. Geophys.* **48**, RG4004 (2010).

5. Coumou, D. & Rahmstorf, S. A decade of weather extremes. *Nat. Clim. Change* **2**, 491–496 (2012).
6. Oliver, E. et al. Longer and more frequent marine heat waves over the past century. *Nat. Commun.* **9**, 1324 (2018).
7. Moron, V., Oueslati, B., Pohl, B., Rome, S. & Janicot, S. Trends of mean temperatures and warm extremes in northern tropical Africa (1961–2014) from observed and PPCA-reconstructed time series. *J. Geophys. Res.—Atmos.* **121**, 5298–5319 (2016).
8. Smale, D. et al. Marine heat waves threaten global biodiversity and the provision of ecosystem services. *Nat. Clim. Change* **9**, 306–312 (2019).
9. Mukherjee, S. & Mishra, A. K. Increase in compound drought and heatwaves in a warming world. *Geophys. Res. Lett.* **48**, e2020GL090617 (2021).
10. Zheng, Z., Zhao, L. & Oleson, K. W. Large model structural uncertainty in global projections of urban heat waves. *Nat. Commun.* **12**, 1–9 (2021).
11. Niedzielski, T. Chapter two. El Niño/Southern Oscillation and selected environmental consequences. *Adv. Geophys.* **55**, 77–122 (2014).
12. Seager, R. & Hoerling, M. Atmosphere and ocean origins of North American droughts. *J. Clim.* **27**, 4581–4606 (2014).
13. Murari, K., Sahana, A., Daly, E. & Ghosh, S. The influence of the El Niño Southern Oscillation on heat waves in India. *Meteorol. Appl.* **23**, 705–713 (2016).
14. Zhou, Y. & Wu, Z. Possible impacts of mega-El Niño/Southern Oscillation and Atlantic multidecadal oscillation on Eurasian heatwave frequency variability. *Q. J. R. Meteorol. Soc.* **142**, 1647–1661 (2016).
15. Zhou, C., Wang, K., Dan, Q. & Tan, J. Attribution of a record-breaking heatwave event in summer 2017 over the Yangtze River Delta. *Bull. Am. Meteorol. Soc.* **100**, S97–S103 (2019).
16. Luo, M. & Lau, N. C. Amplifying effect of ENSO on heat waves in China. *Clim. Dyn.* **52**, 3277–3289 (2019a).
17. Russo, S. et al. Magnitude of extreme heat waves in present climate and their projection in a warming world. *J. Geophys. Res.—Atmos.* **119**, 500–512 (2015).
18. Feng, M., Xing, Y., Yang, J. & Peng, J. Unprecedented Europe heat in June–July 2019: risk in the historical and future context. *Geophys. Res. Lett.* **47**, e2020GL087809 (2020).
19. Ding, Y. et al. Detection, causes and projection of climate change over China: an overview of recent progress. *Adv. Atmos. Sci.* **24**, 954–971 (2007).
20. Zhou, B., Xu, Y., Wu, J., Dong, S. & Shi, Y. Changes in temperature and precipitation extreme indices over China: analysis of a high-resolution grid dataset. *Int. J. Climatol.* **36**, 1051–1066 (2016).
21. Luo, M. et al. Observed heatwave changes in arid northwest China: physical mechanism and long-term trend. *Atmos. Res.* **242**, 105009 (2019).
22. Piao, S. et al. The impacts of climate change on water resources and agriculture in China. *Nature* **467**, 43–51 (2010).
23. Wang, W. et al. Bayesian multi-model projection of irrigation requirement and water use efficiency in three typical rice plantation region of China based on CMIP5. *Agric. For. Meteorol.* **232**, 89–105 (2017).
24. Almazroui, M. et al. Projected changes in climate extremes using CMIP6 simulations over SREX regions. *Earth Syst. Environ.* **5**, 481–497 (2021).
25. Sun, Y. et al. Rapid increase in the risk of extreme summer heat in eastern China. *Nat. Clim. Change* **4**, 1082–1085 (2014).
26. Kang, S. & Eltahir, E. A. B. North China Plain threatened by deadly heat waves due to climate change and irrigation. *Nat. Commun.* **9**, 2894–2899 (2018).
27. Li, X. et al. Concurrent droughts and hot extremes in northwest China from 1961 to 2017. *Int. J. Climatol.* **39**, 2186–2196 (2018).
28. Li, H., He, S., Gao, Y., Chen, H. & Wang, H. North Atlantic modulation of inter-decadal variations in hot drought events over Northeastern China. *J. Clim.* **33**, 4315–4332 (2020).
29. Wei, J. et al. Heat wave variations across China tied to global SST modes. *J. Geophys. Res.—Atmos.* **125**, e2019JD031612 (2020).
30. Xing, W., Han, W. & Zhang, L. Improving the prediction of western North Pacific summer precipitation using a Bayesian dynamic linear model. *Clim. Dyn.* **55**, 831–842 (2020).
31. Wang, B. et al. Northern hemisphere summer monsoon intensified by mega-El Niño/southern oscillation and Atlantic multidecadal oscillation. *Proc. Natl Acad. Sci. USA* **110**, 5347–5352 (2013).
32. Zhang, R., Min, Q. & Su, J. Impact of El Niño on atmospheric circulations over East Asia and rainfall in China: Role of the anomalous western North Pacific anticyclone. *Sci. China Earth Sci.* **60**, 1124–1132 (2017).
33. Huang, D. et al. Contributions of different combinations of the IPO and AMO to recent changes in winter East Asian Jets. *J. Clim.* **32**, 1607–1626 (2019).
34. Xie, S. P. et al. Indo-western Pacific Ocean capacitor and coherent climate anomalies in post-ENSO summer: a review. *Adv. Atmos. Sci.* **33**, 411–432 (2016).
35. Chen, W. et al. Recent progress in studies of the variabilities and mechanisms of the East Asian Monsoon in a changing climate. *Adv. Atmos. Sci.* **36**, 887–901 (2019).
36. Zhang, X. & Han, W. Effects of climate modes on interannual variability of upwelling in the tropical Indian Ocean. *J. Clim.* **33**, 1547–1573 (2020).
37. McPhaden, M. J., Santoso, A. & Cai, W. Understanding ENSO in a changing climate. *Eos* **100**, <https://doi.org/10.1029/2019EO124159> (2019).
38. Boucharel, J., Jin, F.-F., England, M. H. & Lin, I. I. Modes of hurricane activity variability in the eastern Pacific: implications for the 2016 season. *Geophys. Res. Lett.* **43**, 358–366 (2016).
39. Enfield, D. B., Mestas-Nunez, A. M. & Trimble, P. J. The Atlantic Multidecadal Oscillation and its relationship to rainfall and river flows in the continental U.S. *Geophys. Res. Lett.* **28**, 2077–2080 (2001).
40. Rayner, N. A. et al. Global analyses of sea surface temperature, sea ice, and night marine air temperature since the late nineteenth century. *J. Geophys. Res.* **108**, 4407 (2003).
41. Saji, N. H. & Yamagata, T. Possible impacts of Indian Ocean Dipole mode events on global climate. *Clim. Res.* **25**, 151–169 (2003).
42. Henley, B. J. et al. A Tripole Index for the Interdecadal Pacific Oscillation. *Clim. Dyn.* **45**, 3077–3090 (2015).
43. Zhang, X. & Church, J. A. Sea level trends, interannual and decadal variability in the Pacific Ocean. *Geophys. Res. Lett.* **39**, L21701 (2012).
44. Han, W. et al. Intensification of decadal and multi-decadal sea level variability in the western tropical Pacific during recent decades. *Clim. Dyn.* **43**, 1357–1379 (2014).
45. Huang, B., Thome, P. W., Banzon, V. F. & Boyer, T. Extended Reconstructed Sea Surface Temperature Version 5 (ERSSTv5), upgrades, validations, and inter-comparisons. *J. Clim.* **30**, 8179–8205 (2017).
46. Kalnay, E. et al. The NCEP/NCAR 40-year reanalysis project. *Bull. Am. Meteorol. Soc.* **77**, 437–472 (1996).
47. Hersbach, H. et al. The ERA5 global reanalysis. *Q. J. R. Meteorol. Soc.* **146**, 1999–2049 (2020).
48. Fischer, E. & Schär, C. Consistent geographical patterns of changes in high-impact European heatwaves. *Nat. Geosci.* **3**, 398–403 (2010).
49. White, C., Hudson, D. & Alves, O. ENSO, the IOD and the intraseasonal prediction of heat extremes across Australia using POAMA-2. *Clim. Dyn.* **43**, 1791–1810 (2013).
50. Sharma, S. & Mujumdar, P. Increasing frequency and spatial extent of concurrent meteorological droughts and heat waves in India. *Sci. Rep.* **7**, 15582 (2017).
51. Nairn, J., Fawcett, R. & Ray, D. Defining and predicting Excessive Heat events, a National system. In 'Modelling and Understanding High Impact Weather': Extended Abstracts of the Third CAWCR Modelling Workshop, (ed. Hollis, A. J.) 83–86 (CAWCR Tech. Rep. 017, Melbourne, Australia, 2009).
52. Perkins, S. & Alexander, L. On the measurement of heat waves. *J. Clim.* **26**, 4500–4517 (2013).
53. Perkins, S., Alexander, L. & Nairn, J. Increasing frequency, intensity and duration of observed global heat waves and warm spells. *Geophys. Res. Lett.* **39**, L20714 (2012).
54. Perkins, S. E., Argüeso, D. & White, C. J. Relationships between climate variability, soil moisture, and Australian heatwaves. *J. Geophys. Res.—Atmos.* **120**, 8144–8164 (2015).
55. Nairn, J. & Fawcett, R. The excess heat factor: a metric for heatwave intensity and its use in classifying heatwave severity. *Int. J. Environ. Res. Public Health* **12**, 227–253 (2015).
56. Nairn, J., Ostendorf, B. & Bi, P. Performance of excess heat factor severity as a global heatwave health impact index. *Int. J. Environ. Res. Public Health* **15**, 2494 (2018).
57. Asong, Z. E., Khaliq, M. N. & Wheeler, H. S. Regionalization of precipitation characteristics in the Canadian prairie provinces using large-scale atmospheric covariates and geophysical attributes. *Stoch. Environ. Res. Risk Assess.* **29**, 875–892 (2015).
58. Goyal, M. K. & Sharma, A. A fuzzy c-means approach regionalization for analysis of meteorological drought homogeneous regions in western India. *Nat. Hazards* **84**, 1–17 (2016).
59. Roubens, M. Fuzzy clustering algorithms and their cluster validity. *Eur. J. Oper. Res.* **10**, 294–301 (1982).
60. Bensaid, A. M. et al. Validity-guided (Re) clustering with applications to image segmentation. *IEEE Trans. Fuzzy Syst.* **4**, 112–123 (1996).
61. Xie, X. L. & Beni, G. A validity measure for fuzzy clustering. *IEEE Trans. Pattern Anal. Mach. Intell.* **13**, 841–847 (1991).
62. Pettitt, A. N. A non-parametric approach to the change-point problem. *J. R. Stat. Soc.* **28**, 126–135 (1979).
63. Gao, T., Wang, H. J. & Zhou, T. Changes of extreme precipitation and nonlinear influence of climate variables over monsoon region in China. *Atmos. Res.* **197**, 379–389 (2017).
64. Lu, C., Ye, J., Wang, S., Yang, M. & Mao, J. An unusual heat wave in north China during midsummer, 2018. *Front. Earth Sci.* **8**, 238 (2020).

65. Petris, G., Petrone, S. & Campagnoli, P. *Dynamic Linear Models with R* 31–84 (Springer, 2009).
66. Han, W. et al. Decadal variability of the Indian and Pacific Walker cells since the 1960s: do they covary on decadal time scales? *J. Clim.* **30**, 8447–8468 (2017).
67. Han, W. et al. Multi-decadal trend and decadal variability of the regional sea level over the Indian Ocean since the 1960s: roles of climate modes and external forcing. *Climate* **6**, 51 (2018).
68. Roeckner, E. et al. *The Atmospheric General Circulation Model ECHAM-4: Model Description and Simulation of Present-day Climate*. Max Planck Institute for Meteorology Report 218 (Max Planck Institute for Meteorology, 1996).
69. Zhang, L., Han, W., Li, Y. & Shinoda, T. Mechanisms for generation and development of Ningaloo Niño. *J. Clim.* **31**, 9239–9259 (2018).
70. Zhang, L. & Han, W. Impact of Ningaloo Niño on tropical Pacific and an interbasin coupling mechanism. *Geophys. Res. Lett.* **45**, 300–309 (2018).
71. Zhang, L. et al. Indian Ocean warming trend reduces Pacific warming response to anthropogenic greenhouse gases: an interbasin thermostat mechanism. *Geophys. Res. Lett.* **46**, 10882–10890 (2019).
72. Zhang, L. & Han, W. Indian Ocean Dipole leads to Atlantic Niño. *Nat. Commun.* **12**, 5952 (2021).

ACKNOWLEDGEMENTS

This work was jointly supported by the National Natural Science Foundation of China (U2240218, 51979071) and the Fundamental Research Funds for the Central Universities (B230201039). L.Z. is supported by the development fund of the South China Sea Institute of Oceanology of the Chinese Academy of Sciences SCSIO202203 and the State Key Laboratory of Tropical Oceanography grant LTORC2201. Cordial thanks are extended to the editor, associate editor, and anonymous reviewers for their critical and constructive comments, which highly improve the quality of the manuscript.

AUTHOR CONTRIBUTIONS

Conceptualization: W.G.W., W.Q.H. Methodology: J.W., W.Q.H., W.G.W., L.Z., B.R. Investigation: J.W., W.Q.H., W.G.W., L.Z. Visualization: J.W., W.Q.H., W.G.W., L.Z. Supervision: W.G.W., W.Q.H. Writing—original draft: J.W. Writing—review & editing:

W.G.W., W.Q.H., L.Z., B.R. All authors commented on and approved the final version of this manuscript.

COMPETING INTERESTS

The authors declare no competing interests.

ADDITIONAL INFORMATION

Supplementary information The online version contains supplementary material available at <https://doi.org/10.1038/s41612-023-00428-w>.

Correspondence and requests for materials should be addressed to Weiguang Wang.

Reprints and permission information is available at <http://www.nature.com/reprints>

Publisher's note Springer Nature remains neutral with regard to jurisdictional claims in published maps and institutional affiliations.



Open Access This article is licensed under a Creative Commons Attribution 4.0 International License, which permits use, sharing, adaptation, distribution and reproduction in any medium or format, as long as you give appropriate credit to the original author(s) and the source, provide a link to the Creative Commons license, and indicate if changes were made. The images or other third party material in this article are included in the article's Creative Commons license, unless indicated otherwise in a credit line to the material. If material is not included in the article's Creative Commons license and your intended use is not permitted by statutory regulation or exceeds the permitted use, you will need to obtain permission directly from the copyright holder. To view a copy of this license, visit <http://creativecommons.org/licenses/by/4.0/>.

© The Author(s) 2023